Acta Astronautica 221 (2024) 206–217

Contents lists available at ScienceDirect

Acta Astronautica

journal homepage: www.elsevier.com/locate/actaastro

3D printing of shape memory Alloys for complex architectures of smart structures

T. Biasutti [a,*], P. Bettini [b], A. Nespoli [c], A.M. Grande [b], T. Scalia [d], M. Albano [e], B.M. Colosimo [a], G. Sala [b]

[a] Department of Mechanical Engineering, Politecnico di Milano, via La Masa 1, 20156, Milan, Italy
[b] Department of Aerospace Engineering, Politecnico di Milano, via La Masa 34, 20156, Milan, Italy
[c] National Research Council, Institute of Condensed Matter Chemistry and Technologies for Energy (CNR-ICMATE), via G. Previati 1/e, 23900, Lecco, Italy
[d] Italian Space Agency, Technology Unit, via del Politecnico, 00133, Roma, Italy
[e] Italian Space Agency, Space Transportation and in Orbit Servicing Unit, via del Politecnico, 00133, Roma, Italy

ARTICLE INFO

Keywords:
Shape memory alloys
Laser powder bed fusion
NiTi
Damping
Additive manufacturing
Pseudoelasticity

ABSTRACT

Shape Memory Alloys (SMA) are materials used to design smart structures with intrinsic functional properties and improved efficiency. This is a key aspect of aerospace industry and makes SMA good candidates in this field. One of the most widespread SMA is the equiatomic NiTi alloy which, however, has the strong limitation of poor machinability, so only simple shapes can be obtained. Additive Manufacturing processes allow to overcome this limit and to design complex shapes. Compared to other metallic materials, the optimization of the process for NiTi alloy is complicated because, beside mechanical properties and presence of defects, considerable attention needs to be dedicated to the material functionality. The high temperatures involved in the additive process significantly affect the material properties due to possible evaporation of Ni and formation of precipitates that enable a shift of the phase transformation temperatures. This paper is focused on the optimization of the process parameters of the NiTi alloy printed through the Laser Powder Bed Fusion (L-PBF) to ensure optimal pseudoelastic behaviour, which is essential for the design of structural dampers. This was accomplished starting from simple structures and then designing a damper that couples the pseudoelasticity of NiTi with load support capacity.

The L-PBF is a powder-bed technique that selectively melts layers of micrometric metal powder. A pseudoelastic NiTi powder with 50.8 at. % of Ni content was selected and characterized through scanning electron microscope (SEM) and observations connected to an Energy Dispersive X-ray Spectroscopy (EDX) probe. After that, some cubic samples were manufactured, with the dimension of $3 \times 3 \times 15$ mm^3. A set of different laser powers and scanning speeds were used to find the set of process parameters that optimize the functional properties of the printed parts. Near fully dense specimens with density higher than 99.5 % were selected for further investigations. Differential scanning calorimetry (DSC) and mechanical tests were performed on as-built and heat-treated samples.

Quasi-static mechanical tests were accomplished in compression mode, at different strains, up to 8 %. It was observed that the residual strain for cyclic loading at 4 % is lower than 1 %, so good recovery of the deformation was shown. Moreover, numerical analyses that mimic the pseudoelastic behaviour in compression tests were implemented.

Finally, the best set of parameters was selected on the basis of the material's ability to recover deformations and its loss factor.

* Corresponding author.
E-mail addresses: tiziana.biasutti@polimi.it (T. Biasutti), paolo.bettini@polimi.it (P. Bettini), adelaide.nespoli@cnr.it (A. Nespoli), antoniomattia.grande@polimi.it (A.M. Grande), tanya.scalia@asi.it (T. Scalia), marta.albano@asi.it (M. Albano), biancamaria.colosimo@polimi.it (B.M. Colosimo), giuseppe.sala@polimi.it (G. Sala).

https://doi.org/10.1016/j.actaastro.2024.05.024
Received 12 January 2024; Received in revised form 2 May 2024; Accepted 15 May 2024
Available online 27 May 2024

Nomenclature

W	Loss energy, area between loading and unloading curve in mechanical test
$W_{loading}$	Energy stored in loading path
μ	Loss factor
ε	Strain
A_S	Austenite Start Temperature
A_F	Austenite Finish Temperature
M_S	Martensite Start Temperature
M_F	Martensite Finish Temperature
MVF	Martensite Volumetric Fraction
E	Energy Density
P	Laser Power
v	Scanning Speed
h	Hatch Distance
t	Layer Thickness
ρ_{meas}	Measured density
ρ%	ρ_{meas} and bulk density ratio percentage
Acronyms/Abbreviations	
AM	Additive Manufacturing
SMA	Shape Memory Alloys
NiTi	NiTiNOL
L-PBF	Laser Powder Bed Fusion
DSC	Differential Scanning Calorimetry
SEM	Scanning Electron Microscope
EDX	Energy Dispersive X-ray Spectroscopy
AB	As Built
HT	Heat Treatment
at. %	Atomic percentage

1. Introduction

Shape Memory Alloys (SMA) are functional materials extensively studied for various applications in different industries such as aerospace, automotive and biomedical. They exhibit a reversible transformation between two solid phases stable at different temperature ranges, austenite, stable at high temperatures and martensite stable at low temperatures, that drives the two main material effects: pseudoelasticity and shape memory. One of the most widespread SMA is the equiatomic Nickel–Titanium (NiTi). This material shows remarkable advantages when used as sensor, actuator or damper. Among these, there is its low power-to-weight ratio; the possibility of being embedded directly in the structure and the consequent compactness of the system, which is especially important for aerospace applications; its biocompatibility, required for biomedical applications; and its fatigue behaviour in both thermal and mechanical cycling conditions. However, a limitation of NiTi is that with traditional technologies it has a poor workability, allowing the manufacturing only of very simple geometries, such as wires, springs, plates or combinations of these. Therefore, research is focusing on different technologies, such as Additive Manufacturing (AM), to enable the design of complex NiTi structures. In this way, it is possible to expand the applications of these materials, exploiting their functionality and their advantages.

Laser Powder Bed Fusion (L-PBF) is one of the most studied AM technologies for NiTi structure manufacturing. Most of the published works focus on the study of process parameters that best optimized the functional properties of the printed specimens [1–5]. Indeed, the fundamental aspects that characterize the mechanical behaviour of the material, and therefore its functionality, are the percentage of Ni and Ti and the thermal history that the material undergoes during the production. The energy input is one of the main criterions used to study the L-PBF process as it counts for the main process parameters. It is usually calculated using eq. (1), where P is the laser power, v is the scanning speed, h is the hatch distance, t is the layer thickness. Several works established an optimal range of laser energy density eq. (1) between 55 and 222 J/mm^3 to reduce presence of defects and reach good density. The process parameters and so the laser energy density have an important role in the evaporation of Ni during the manufacturing and in the formation of precipitates. These two factors in fact strongly influence the transformation temperatures of the material and consequently its functionality. Moghaddam [1] for example, studied the variation of hatch distance to compare the different thermal and mechanical behaviour and the microstructure of the samples manufactured. Nespoli [2] instead evaluated the variation of density and mechanical response of structures manufactured with fixed laser power and varying scan speed and hatch distance. Wang [3] linked the variation of transformation temperatures to the variation of parameters. In this case, the scanning speed was varied between 400 and 1200 mm/s, the hatch distance from 40 to 110 μm and the laser power from 60 to 200 W. Saedi [4] compared pseudoelastic behaviour and microstructure of samples in which laser power was set between 100 and 250 W and scanning speed between 125 and 1500 mm/s. A detailed list of the most diffused parameters in literature at different powder composition was collected by Mojtaba in Ref. [5].

$$E = \frac{P}{v * h * t} \quad 1)$$

A further important aspect to consider is the defects formation in samples during the production process. Some analytical models based on the prediction of the melt pool dimensions were used by Zhu [6] and Xue [7]. These models calibrated on specific NiTi powder (50.1 at.% of Ni and 50.8 at.% of Ni) allowed for the definition of printability maps free of defects. Both Zhu and Xue identified in the maps some areas defined by process parameters that enables defects, such as keyholes were ascribed to high laser power and low scanning speed, the balling effect was related to high laser power and high scanning speed, higher than 1500 mm/s, and lack of fusion defects was detected at low laser power and high scanning speed. In both researches, some samples with different printing parameters inside and outside the optimal area were manufactured and studied through thermal and mechanical analyses and by microscope observations.

Since the NiTi behaviour highly depends on the material thermal history, so an important aspect is the effects of thermal treatment on the sample transformation temperatures. Saedi [8] for example studied two different aging temperatures, 350 C and 450 C, and duration time between 5 min and 18 h. By comparing DSC signals of the as-built specimens and the starting powder, Saedi observed that the transformation temperatures shift to higher valued with the increasing of the treatment time. Moreover, Saedi confirmed that with the thermal treatment it is possible to tailor the functionality of the structure manufactured, adapting the printed specimens to the final application and the working temperatures. In Ref. [9] instead, Saedi studied the effects of the increase of the heat treatment temperature fixing the duration time at 30 min, 1 h and 1.5 h.

One of the main NiTi effects that can be used for space applications is pseudoelasticity, which consists in the recovery of large deformations, up to 8 %, through a mechanical hysteresis ascribed to the transition of austenite into a stress-induced martensite during loading and of martensite into austenite during unloading. This effect is suitable for the design of damping structure. Indeed, the transformation from the initial austenite phase to the following martensite phase due to the increase of stresses, shows damping properties for strains between 4 % and 8 %. At low stain (10^{-5}) the damping ability of the material is associated to the internal friction during transformation of phase due to variation of temperatures [10]. Nespoli [11] studied the loss factor of various NiTi samples manufactured with different printing parameters by L-PBF. The research compared the mechanical behaviour of the materials tested in quasi-static and dynamic conditions at 0.5 Hz, 1 Hz and 10 Hz. Nespoli moreover, compared the loss factor obtained with the ones of other materials. Also in this case, a correlation between the process parameters and the damping ability of the material has been identified, defining damping maps.

Nowadays, most of the complex structures fabricated via additive manufacturing have been designed for medical applications, in particular for prostheses and biomedical implants. Jahadakbar [12] for

example designed a NiTi plate for bone fixation, tailoring the stiffness of the structure and the porosity to best match the junction bone-plate. Bartolomeu [13] similarly focused on design and manufacturing of lattice structure with different dimensions, porosity and cell geometries. The structures show elastic modulus similar to the bone one, indicating the possibility to use it for orthopedic implants. These examples, although restricted to the biomedical filed, confirmed the possibility to use Additive Manufacturing technologies to produce complex structures tailored to the specific application and exhibiting the functionality of SMA materials.

Based on the research done so far, damping ability of SMA can be used to design structures able to absorb dynamic loads in specific space conditions, avoiding presence of complex heavy kinematic solutions and implementing a simple and compact one. Before implementing this, it is necessary to find the best set of parameters for the starting powder. In this paper, different printing parameters were set based on mapping regions defined in published studies that worked with NiTi powder with similar composition to that considered in the present work: 50.8 at.% of Ni [6,7]. Initially, the manufactured specimens were observed through optical microscope to find the set of parameters that allows to avoid as much as possible presence of defects. After that, the specimens with the lowest number of defects were mechanically tested in static conditions and compared with each other to assess their ability to recover strain and the related loss factors. Moreover, a numerical model mimicking the mechanical behaviour of one tested specimen was implemented to verify the possibility to simulate with adequate confidence the behaviour of the NiTi material manufactured by L-PBF technologies. The validated model can be used for future design of more complex structures fabricated with the same set of printing parameters. The final goal of this research was to assess the best manufacturing parameter set that enables maximizing the damping ability of the material and its ability to fully recover strain upon load.

As reported, the process parameters have a great influence on the variation of the material composition and consequently on its final performance. Various parameter sets have been tested in the literature with the aim of finding a set that can improve the material's functionality. At present, in our knowledge, most of the works focus on machines with continuous laser. This research aims to contribute to the ongoing investigation into the printability of NiTi by studying the influence of process parameters using a pulsed laser machine.

2. Material and methods

The NiTi powder used in this study was gas atomized and supplied by Nanoval GmbH. The particle's size is between 10 and 50 μm and the reported d_{50} is 24.5 μm.

The NiTi specimens were manufactured through the AM400 of Renishaw on a NiTi platform and in a reduced build volume (78 × 78 × 55 mm^3). The machine works with a 400 W Ytterbium fibre laser in pulsed wave emission producing a spot diameter of approximately 70 μm at the focal point. During the printing process, the building chamber was maintained in a controlled argon atmosphere with oxygen content lower than 500 ppm. No preheating was applied to the build platform. In this research, the layer thickness, the laser point-to-point distance *d* and the hatch distance were kept constant respectively at 30 μm, 60 μm and 120 μm. Besides, the laser power and the laser exposure time were varied accordingly to data listed in Table 1. The table also report the scanning speed, that was calculated as the ratio between the laser point-to-point distance *d* and the laser exposure time *t*, and the energy density calculated through eq. (1). The data listed in Table 1 identify the 12 families F1–F12 of process parameters considered in the present work. For each family three specimens 3 × 3 × 15 mm^3 were manufactured with the main axis parallel to the building direction. In general, L-PBF process requires parts to be supported to sustain overhanging surfaces, to remove heat away from the parts and to reduce geometrical distortions. In this work, being the printed parts with simple geometry, 3 mm supports were introduced to promote the heat transfer and to easily remove the samples at the end of the printing process without damaging it, see Fig. 1.

Table 1
Printing parameters.

F	Laser Power [W]	Scanning speed [mm/s]	Time of scanning [μs]	Energy density [J/mm^3]
1	75	125	480	166.67
2	75	250	240	83.33
3	100	125	480	222.22
4	100	250	240	111.11
5	100	500	120	55.55
6	125	500	120	69.44
7	125	750	80	46.29
8	150	750	80	55.55
9	150	1000	60	41.67
10	175	1000	60	48.61
11	175	1250	48	38.89
12	200	1250	48	44.44

Hatch distance: 120 μm.
Layer thickness: 30 μm.
Laser point-to-point distance: 60 μm.

The NiTi powder's transformation temperatures were investigated through DSC analysis by the Q100 of TA Instruments. Furthermore, a batch of powder was observed by SEM (LEO 1430) to verify the particle dimensions. The chemical composition was estimated with EDX (INCA ENERGY 200 Oxford Instrument).

The density was selected as the key factor to identify the sets of parameters among those selected, that enable near-fully dense parts. In this work we considered the measured density (ρ_{meas}), and ρ% that is the percentage ratio between ρ_{meas} and bulk density (6.45 g/cm^3 [14]). It was assumed that the optimal process parameter set was the one that allowed to obtain ρ% higher than 99.5 %. The ρ_{meas} was measured using the Archimedes' principle through an analytical balance (Gibertini E50/S2). Three measurements per family were performed.

Defects' analysis was accomplished through light optical microscope (LeitzAristomet) observations. To this end, two specimens for each parameters' set were embedded in circular epoxy resin moulds in longitudinal and transverse position to observe the defects respectively along and perpendicularly the main axis, as visible in Fig. 2. Each sample was mechanically polished with abrasive papers from 180 to 1200 grit. For samples longitudinally embedded, five sections placed at different sample height were observed, trying to keep the observation points equally spaced so that almost the entire sample could be analysed. Transversely embedded samples, instead, were only observed in one section, approximately in the middle of the thickness. Furthermore, after polishing, the latter samples were etched for 20 s in a solution of 3 % HF + 12 % HNO_3 + 85 % H_2O for revealing the grain boundaries and morphology. Defects' analysis was employed to identify the process families that enable defect free specimens. A comparison between results of defects' analysis and density measurements obtained both through image and Archimedean analysis was also performed.

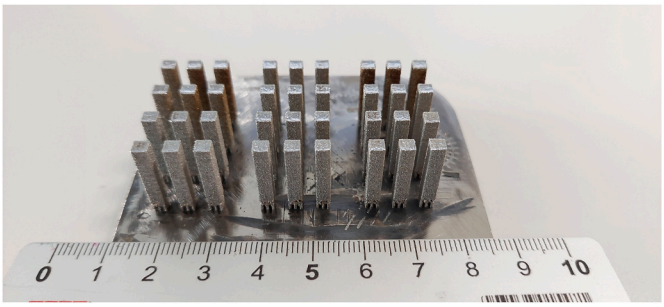

Fig. 1. Manufactured specimens with the 12 set of parameters.

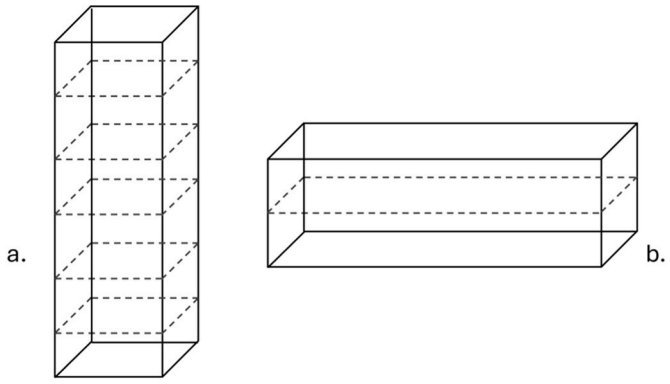

Fig. 2. Representation of embedded sample and section analysed through optical microscope. a. Longitudinal embedded sample b. Transverse embedded sample.

DSC analysis (Q100, Ta Instruments) was performed at a heating/cooling rate of 10 °C/min in the range from −100 °C to 100 °C on 10–40 mg samples. The transformation temperatures were calculated with the Universal Analysis software (TA Instruments) using the tangents methods. For each selected families, DSC measurement was performed on the as-build, solubilised and thermal treated specimens. The solubilization and the heat ageing treatments were accomplished in sealed quartz tube for 5.5 h at 950 °C, and in air at 450 °C for 15 min, respectively. A final water quench was considered for both the heat treatments.

Both as-built and heat treated samples were tested in quasi-static compression condition through an MTS 2/M machine (10 kN load cell), in a thermal chamber at $A_F + 10$ C temperature. The quasi-static compression tests were made in displacement control mode at 0.250 mm/min and during the test an extensometer was attached to the grips to calculate the strain. Before testing, the sample's height was reduced to approximately 5 mm to avoid buckling. This process was performed by cutting the sample using a cutting machine and smoothing the surfaces so that the upper and the lower faces were parallel. This last step was performed by polishing the samples with 180 grit sandpaper. Each test was composed by five cycles at 4 % strain. After the compression at 4 %, the specimens were tested at 5 % and then 6 %, starting in both cases from the residual strain of the previous test. A prestress of 15 MPa was considered for all the measurements.

The loss factor at last loading-unloading cycle of the 4 % strain test, was calculated to compare the damping ability of the different families. The loss factor was calculated through the following equation:

$$\eta = \frac{W}{2 * \pi * W_{loading}} \quad 2)$$

Finally, a preliminary numerical model that simulate the pseudoelastic behaviour of the material was implemented on Abaqus2020. The real sample dimensions, used as model input, were identified through optical image analysis through the ImageJ open-source software. The model has 4950 C3D8R hexahedral elements. Furthermore, the model temperature input was the one used in the mechanical tests ($A_F + 10$ C). The model, that accounts for geometric non-linearities, has two steps: the first one represents the loading path in which a displacement of 4 % strain was imposed, and the second one mimics the restore to the initial un-loaded conditions. The two steps were composed each one by 10 substeps. The material was modelled using the superelastic material property implemented by Auricchio Model [15]. The input parameters used in the current work were obtained by the mechanical tests and DSC analyses performed during initial experimental phase on the as-built specimen.

3. Results

3.1. NiTi powder characterization

SEM images (Fig. 3a) highlighted that the NiTi powder was composed by a high percentage of particles with small size that have the diameter lower than 25 μm. This can strongly influence the powder flowability during the printing process [16,17]. The EDX performed in the area reported in Fig. 3b showed that the average atomic percentage of Nickel was 51.72 at. % [18,19]. This value confirmed that at room temperature the NiTi powder was pseudoelastic.

3.2. Density and defects analyses

Table 2 reports the densities values measured with Archimedes' method compared with the ones calculated by the microscope images of the polished samples. It can be noticed that the two methods enable similar results. The results of the density analysis showed that the specimens with the highest ρ% belong to F2 and F5 families, with values of 99.6 %. All the other families showed lower values, between 98.1 % and 99.2 %.

However, with respect to the Archimedes' method, the microscope images also highlighted the presence of internal cracks in some specimens (Figs. 4 and 5). It was observed that all samples of families from F6 to F12 present visible intergranular cracks. Furthermore, on the specimens manufactured with lower laser power and scanning speed (F1, F2, F3, F4 and F5), the only defects were gas pores. The average dimension of these defects was between 8 μm and 33 μm.

Moreover, the increase of the laser power and scanning speed resulted in an increased crack thickness and greater propagation along the building direction of the specimen. The families with higher percentage of cracks were F11 and F12, that were the ones with lowest energy density and highest laser power and scanning speed.

Therefore, due to the results of the density measurements, the further mechanical study focused on the F2 and F5 families. In addition, the microscope images analysis suggested us to test also families F1, F3 and F4 since were the one without horizontal cracks.

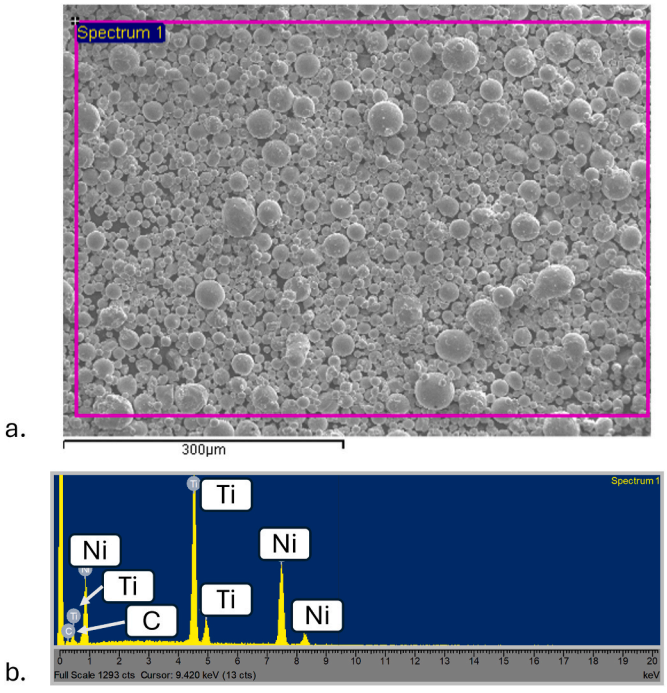

Fig. 3. a. SEM image of the NiTi powder (50.8 at.% of Ni) and b. EDX results on the spectrum reported in a.

Table 2
Specimens density measured using Archimedes' Method and calculated from microscope images.

	Archimedes' method		Microscope images	
	ρ_{meas} [g/cm^3]	ρ% [%]	ρ_{meas} [g/cm^3]	ρ% [%]
1	6.32	98.1	6.34	98.2
2	6.42	99.6	6.43	99.7
3	6.33	98.1	6.34	98.2
4	6.35	98.5	6.37	98.7
5	6.43	99.6	6.42	99.5
6	6.36	98.7	6.34	98.4
7	6.39	99.2	6.40	99.3
8	6.37	98.8	6.36	98.7
9	6.38	98.8	6.35	98.4
10	6.34	98.3	6.36	98.6
11	6.36	98.7	6.37	98.8
12	6.38	98.8	6.35	98.5

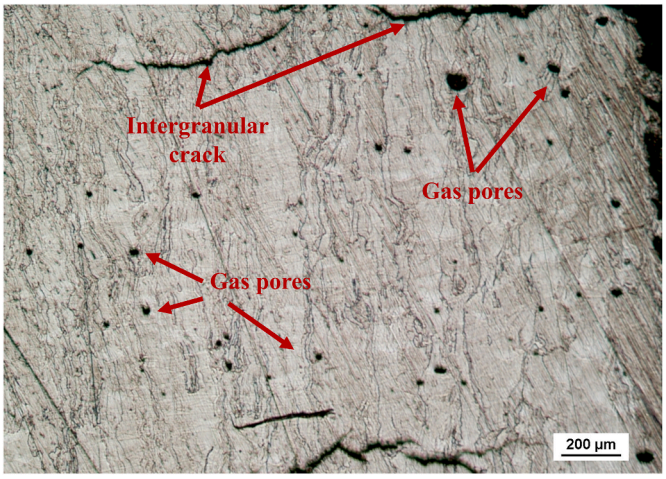

Fig. 4. Optical image of F6 family.

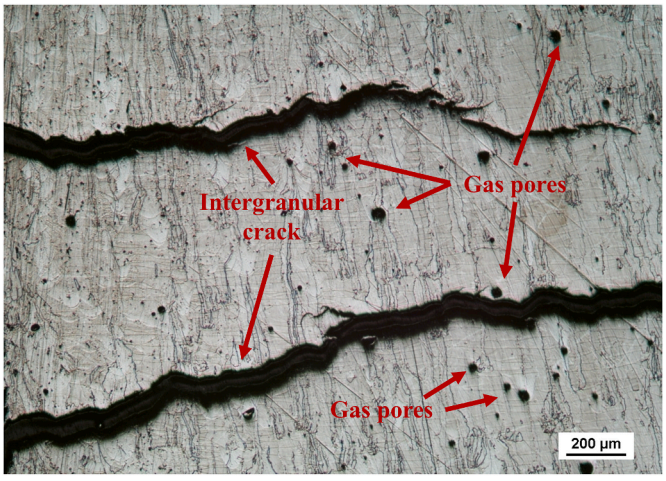

Fig. 5. Optical image of F11 family.

3.3. DSC on powder and printed specimens

The DSC results on powder shows that austenite finish temperature (Fig. 6) was approximately 16 °C, reconfirming the pseudoelastic behaviour of the powder at room temperature. In the cooling curve it was visible a small second peak, probably ascribed to precipitates due to the manufacturing process or also to R-phase [8,9,20,21]. The

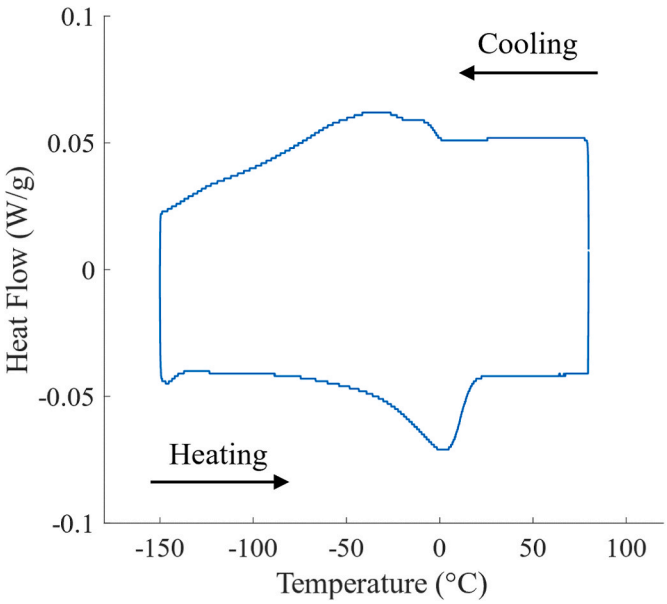

Fig. 6. DSC analysis of the NiTi powder.

transformation temperatures are reported in table below.

Table 3 also reports the phase transformation temperatures of the as-built and heat-treated specimens of F1–F5 families. As noticeable, the thermal treatment enabled a decreasing of the transformation temperatures with respect to as-bult condition [5,8,22]. Furthermore, except for the as-built F5 sample that presented an A_F equal to 8 °C, no one of the other families were pseudoelastic at room temperatures. Specifically, F1 and F3 showed particularly high transformation temperatures, close to 90 C for as-built specimens. Comparing the DSC results with the one of the NiTi powder, it was possible to highlight the change of chemical composition of Ni and Ti percentage, and consequently transformation temperatures, of the material associated to the manufacturing process. As known indeed, the melting process cause Ni evaporation and formation of oxides due to impurities pick-up. These change the NiTi chemical composition compared to the one of the starting powder. The Ni loss seems to be the main effect in F1–F4 families, leading to an increase in transformation temperatures. Instead, for F5 AB the reduction of transformation temperatures compared to the initial powder can be due to formation of oxides and precipitates. These effects are reported in many researches, such as [4,5,8,22,23].

The results highlighted how the usage of different printing parameters induced different transformation behaviours. Even after the solubilization and the aging treatments the differences in transformation temperatures persisted.

The specimens F1 and F3, manufactured with the same scan speed, showed similar transformation temperatures in as-built specimens. After the thermal treatments instead, there was no longer this similarity. In

Table 3
Transformation temperatures of the NiTi powder and of AB and HT samples.

		A_F [°C]	A_S [°C]	M_S[°C]	M_F[°C]
Powder		15.9	−43.6	15.4	−94.2
AB	1	87	22	58	−10
	2	33	−27	−12	−76
	3	91	21	63	−9
	4	39	−7	19	−43
	5	8	−63	4	−107
HT	1	56	7	46	−23
	2	35	−5	30	9
	3	78	9	53	7
	4	37	1	37	−47
	5	39	12	36	3

particular, it was observed an enlargement of the transition peaks, in F1 in the transformation from austenite to martensite, in F3 in the transformation from martensite to austenite.

Fig. 7 reports the DSC heating curves of F2 for as built and thermal treated specimens. As expected, after the solubilization process the transformation peak appeared narrower compared to the one of AB curve due to the homogenisation of the material [7,24]. Furthermore, the thermal treatment led to a slight increase in austenite finish temperature. This was also observed for F5. Instead, all the other families tested exhibited a reduction in TT after heat treatment.

3.4. Mechanical test

The compression tests performed at $A_F + 10$ C highlighted that the five families exhibited different mechanical behaviour. Table 4 shows that the transformation from austenite to stress-induced martensite started at high strain compared to traditionally manufactured structures, in which transformation usually starts at 1–2% [25]. Furthermore, in many NiTi samples manufactured by L-PBF the transformation started after 1 % [1,13]. Other researches, such as [26], show instead the start of phase transformation after 2 % strain, as in results of Table 4. This is particularly evident in families F1, F3 and F5 of heat-treated specimens (see Appendix A).

Furthermore, most of the residual strain was stored during the first cycle and decreased in the following ones with the stabilization of the material. Table 4 reports residual strain at the end of first and fifth cycles of loading-unloading.

The heat-treated families showed a better recovery of deformation. In particular, for families F2, F4 and F5 the residual strain at the end of the fifth cycle was lower than 1 %, exhibiting a good ability of the material to recover strain after removing the external load.

The loss factor was evaluated at the 5th cycle of the 4 % test. Due to the residual strain stored in previous cycles the range of evaluation of η change for each family. The highest η was obtained for F1 family. This was also the specimen that reached the highest stress values during the loading. All the other families present a η in the range from 0.027 to 0.038.

The first cycle in AB samples showed a clear plateau and the transformation for all families started at approximately 500 MPa (see Fig. 8). The stresses for HT samples were lower compared to AB samples (see Fig. 9). F1, F3 and F5 heat-treated families showed that the material was at the beginning of the phase transformation from austenite to martensite, indeed the curve at 4 % just started to change slope.

The graphs concerning the test at higher deformations confirmed the pseudoelastic behaviours detected in samples at 4 %. In particular, F4 HT sample (Fig. 10) showed good strain recovery, with final residual strain less than 1 %. The families that exhibited a reduced ability to recover the deformation at 4 %, such as F1 and F3, continued to show a similar behaviour, both for AB and HT samples. F1 and F3 HT specimens had respectively a final residual strain of 2.86 % and 4.20 % after reaching strain of 6 %.

Table 4
Mechanical results of compression tests of F1–F5.

	F	ε_{trans} [%]	η	$\varepsilon_{residual\ 1st}$ [%]	$\varepsilon_{residual\ 5ft}$ [%]
AB	1	1.78	0.0627	1. 00	1.15
	2	2.82	0.0356	0.61	0.99
	3	1.97	0.0270	1.51	1.88
	4	1.79	0.0347	0.54	0.91
	5	2.58	0.0331	0.27	0.80
HT	1	3.30	0.0430	1.87	2.34
	2	2.58	0.0319	0.67	0.85
	3	3.12	0.0373	1.98	2.29
	4	2.09	0.0385	0.14	0.49
	5	3.12	0.0263	0.16	0.35

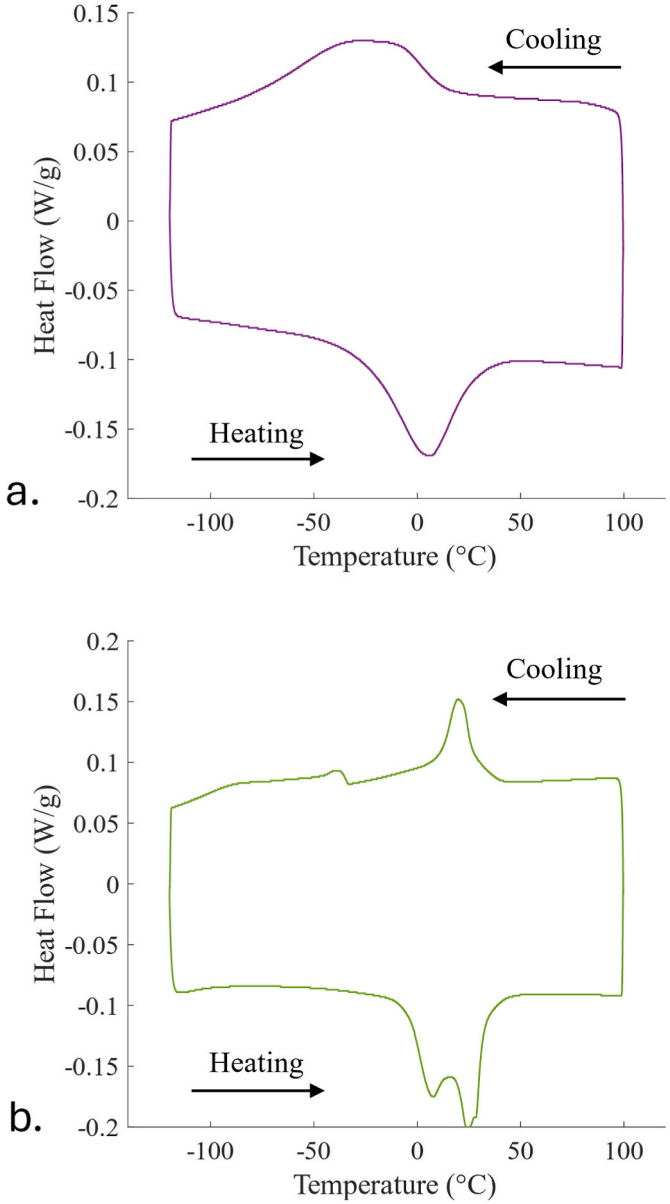

Fig. 7. DSC curve of the: a. as-built and b. heat treated F2 sample.

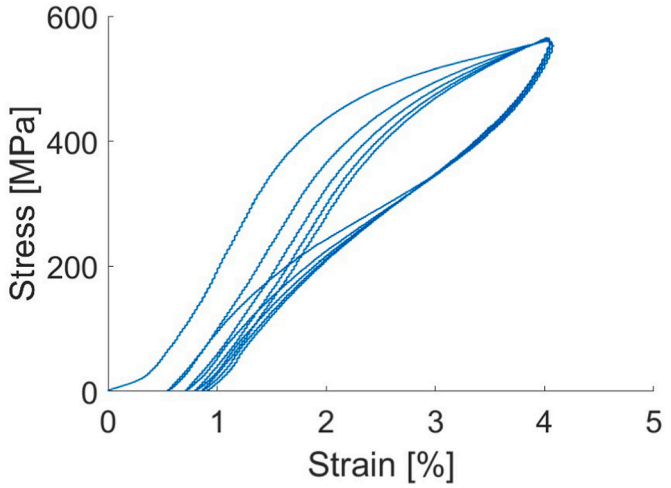

Fig. 8. Compression test at 4 % strain of AB F4.

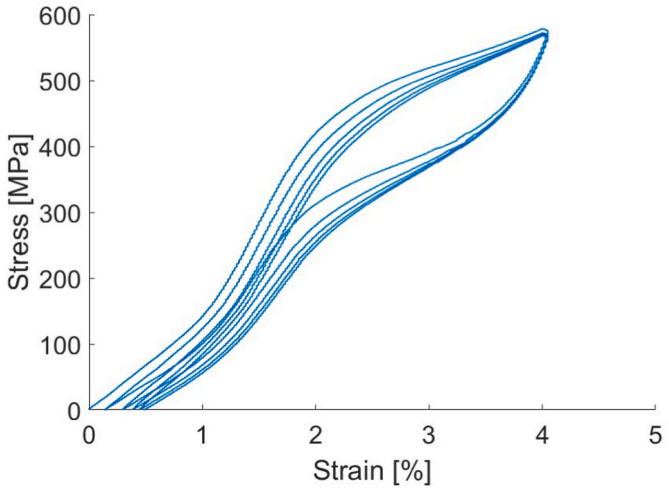

Fig. 9. Compression test at 4 % of HT F4 sample.

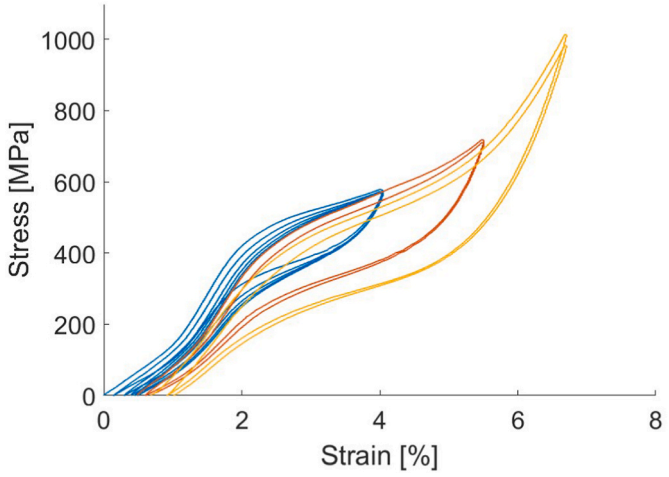

Fig. 10. Compression test at 6 % of HT F4 sample.

3.5. Numerical analyses

Fig. 11 shows the numerical results compared to the experimental one of F4 AB family. It can be noticed that the experimental behaviour was well simulated by the Abaqus model, particularly during the loading curve.

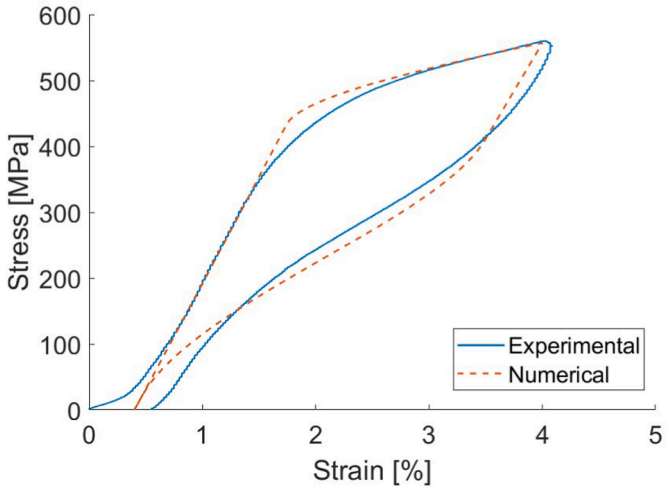

Fig. 11. Experimental and numerical results of compression test of AB F4.

Furthermore, the initial point of numerical curve was intentionally shifted to remove the non-linear part of the experimental results, probably associated to sample and testing machine adjustments.

Moreover, the transformation from austenite to stress-induced martensite started very sharply in the numerical curve. Despite of this, numerical and experimental results presented the same starting point of the phase transformation.

Besides, the unloading curve stresses were underestimate by the numerical model. This was particularly evident in the unloading ”plateau”. Moreover, the implemented model presented the limit of not consider a residual strain at the end of the test, assuming the material already stabilized. Consequently, in the numerical simulation the material recovered completely the deformation applied.

The loss factor calculated from numerical curve was 0.0585, slightly higher than the 0.0560 value obtained by experimental results. This is presumably ascribed to the differences between the two curves, experimental and numerical, especially at the beginning of the phase transformation and during the unloading. In general, the numerical model simulated with a reasonable confidence the material behaviour, also in terms of the loss factor.

Fig. 12 shows the evolution of the martensite volumetric fraction and of the strain during the 4 % test estimated through the numerical model. The unloading started at 0.5 test progression. From the graph is possible to see that not all the material was transformed into martensite at 4 %. The final MVF at loading condition was 0.28. The final MVF test at the end of the simulation was 0, all the material recovered the applied load and returned to the initial condition, as previously discussed. This did not occur in the experimental tests, in which the samples showed a residual strain.

4. Discussion

The high percentage of powder with dimensions below 20 μm significantly affect flowability during manufacturing [16,17]. This could have influenced the presence of defects in the printed samples. Both the DSC, through the transformation temperatures, and EDX, through the average material composition, confirmed that most of the powder was in austenite phase at room temperature, indicating that the starting material had a pseudoelastic behaviour [18–22].

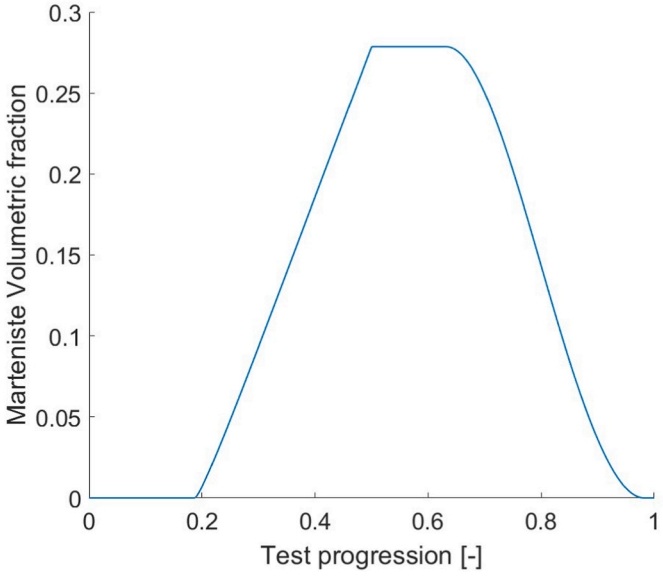

Fig. 12. Martensite Volumetric Fraction during the loading-unloading 4 % test obtained through numerical simulation.

After the manufacturing process, the transformation temperatures shifted to higher values. This could be mainly due to the evaporation of Nickel during the process [22,23]. As a result, except for AB F5, all tested families had A_F higher than room temperature, necessitating the use of a thermal chamber for mechanical testing.

The microscope images showed a clear trend of defect formation. Families obtained with lower laser power and scanning speed showed only presence of pores. Since the size of these defects was less than 50 μm and they were mostly circular, it was possible to assume that they were gas pores [3,6,27]. Possible causes of the formation of these defects are ascribed to gas that was entrapped in original powder during production, or fluctuation of the surface of the melt pool.

Increasing the laser power and the scanning speed, and reducing the energy density, some horizontal cracks appeared. The crack thickness resulted higher in F11 and F12 samples, so when the laser power is higher. Probably the high laser power in these cases could have caused greater problems in heat dissipation leading to residual stresses formation that could induced formation of the horizontal cracks [28]. Moreover, the manufacturing was performed in reduce building platform that couldn't be pre-heated. Consequently, the thermal gradient during printing process may had facilitate the formation of these defects. It is also evident that values that are frequently utilized in the literature [5,8,9], including P = 250 W and v = 1250 mm/s, were inappropriate for this investigation since they caused fracture formation. This may suggest that the printability map of NiTi may change when employing a pulsed laser machine.

The obtained percentage densities were between 98.1 % and 99.6 % when measured with Archimedes' method. The results obtained from images microscope were slightly different but well approximate the experimental ones. The difference between the two methods can be related mainly to the fact that the analysis through microscope images focuses only on a specific sample area while the Archimedes' method considers all the specimen volume. The analysis of defects led to exclude the F6–F12 families from subsequent mechanical analysis.

The mechanical tests showed good pseudoelastic behaviour for almost all set of parameters. The as-built specimens had a clear transformation plateau in the first cycle. The subsequent cycles had a lower area between loading and un-loading curves, this was mainly due to the cycling effect [29–31]. During the stress induced transformation indeed, a redistribution of stresses and dislocations occurs, leading to a decrease of stresses in the curves. The reduction of the area between loading and unloading curves after the first cycles is also associated to the not complete recovery of the first imposed strain. The highest value of loss factor was obtained for the AB F1 but this family showed also a residual strain at the end of the test of 1.15 %. The ability of the material to recover the imposed deformation was one of the main aspects used to evaluate the parameter set and the behaviour of the material. Therefore, even if the loss factor was high in F1 AB, the final residual strain could make it not suitable for our applications. The other families of AB specimens, especially F3 and F5, exhibited narrowed curves and lower loss factors. Moreover, family F3 stored high residual strain in first cycle. The best compromise between damping and functionality of as built specimens were obtained with families F2 and F4.

Even thermal treated specimens showed good pseudoelastic behaviour in families F2 and F4. In these two cases the transformation was clearly visible in both loading and un-loading curves. After the first cycle, the material showed an almost total recover of the deformation and in both cases the residual strain was less than 1 %. In particular, for F4 the solubilization and then the annealing allowed to almost halve the final residual strain, decreasing it from 0.91 % to 0.49 %.

The F1 HT specimen seemed not to show pseudoelastic behaviour, especially compared to other threated families. Probably this can be related to the presence of internal defects. From the microscope images indeed, it was observed presence of pores. In addition, in this case the material almost did not reach the start of the plateau at 4 %. The change of slope characteristic of phase transformation is only approached at 4 % strain. At the end of the test the material showed a residual strain of 2.34 %, so this set of parameters did not allow to reach good deformation recovery behaviour. A similar behaviour was seen in F3 HT specimen. Family F5 HT instead, showed a low residual strain but also a narrowed curved and a low loss factor value.

Comparing the loss factor obtained with ones of other traditional material [11] is possible to highlight the advantages of NiTi pseudoelastic effects and of its employment for damping applications. Therefore, combining the pseudoelastic effect with dedicated geometry even higher damping properties can be reached. For the choice of the best set of parameters it was important not only the loss factor but also the ability of the material to recover the imposed deformation and the pseudoelastic curve obtained from mechanical tests [3,22].

Finally, the differences between numerical and experimental curves could be related mainly to the presence of defects. This one, as voids and cracks, change the distribution of stresses inside the material. The consequence of this is that not all the material transforms at the same time and consequently the global behaviour of the structure, visible in stress-strain curve, is slightly different.

5. Conclusions

The work was meant to find the best set of parameters within twelve different families to produce through a L-PBF machine equipped with a pulse laser, NiTi specimens with good damping property.

Families obtained with high laser power (125 W–200 W) and scan speed in the range from 500 mm/s to 1250 mm/s showed internal cracks. On the other side, when the laser power and the scan speed were in the range respectively from 75 W to 100 W and form 125 mm/s to 500 mm/s, defects were ascribed to porosities. Five families were tested mechanically both in as-built and thermal treated conditions. Results show that the best set of process parameters were those related to the families F2 and F4. In these cases, the material showed good ability to recover the deformation imposed, with residual strain less than 1 %, and high loss factors.

In general, the loss factor calculated for each family demonstrated the good damping ability of the material.

These results encourage the design of damping structure for space application that use NiTi functionality and L-PBF technologies.

CRediT authorship contribution statement

T. Biasutti: Conceptualization, Data curation, Formal analysis, Investigation, Methodology, Software, Visualization, Writing – original draft, Writing – review & editing. **P. Bettini:** Conceptualization, Funding acquisition, Project administration, Resources, Supervision, Validation, Writing – review & editing. **A. Nespoli:** Conceptualization, Investigation, Methodology, Project administration, Resources, Supervision, Validation, Visualization, Writing – review & editing. **A.M. Grande:** Conceptualization, Funding acquisition, Resources, Supervision, Validation, Writing – review & editing. **T. Scalia:** Funding acquisition, Writing – review & editing. **M. Albano:** Funding acquisition, Writing – review & editing. **B.M. Colosimo:** Conceptualization, Funding acquisition, Project administration, Resources, Supervision, Validation, Writing – review & editing. **G. Sala:** Conceptualization, Funding acquisition, Project administration, Resources, Supervision, Validation, Writing – review & editing.

Declaration of competing interest

The authors declare that they have no known competing financial interests or personal relationships that could have appeared to influence the work reported in this paper.

Acknowledgements

The present work has been supported by the collaboration agreement between ASI and Politecnico di Milano "Attività di ricerca e innovazione" n. 2018-5-HH.0.

Appendix A. Compression test results

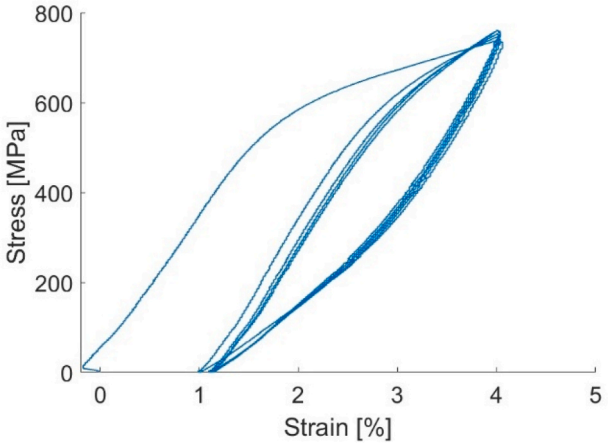

Fig. 13. Compression tests at 4 % of AB F1 sample

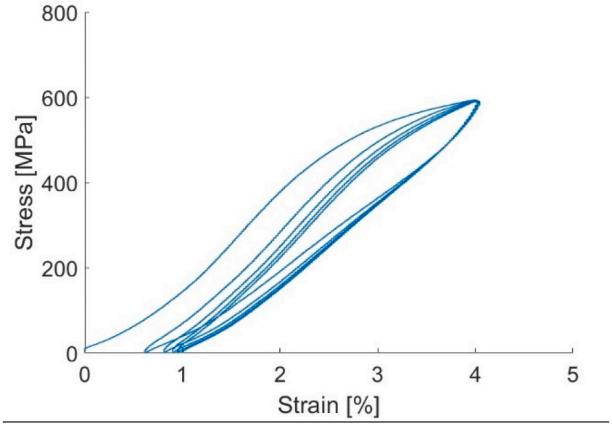

Fig. 14. Compression test at 4 % of AB F2 sample

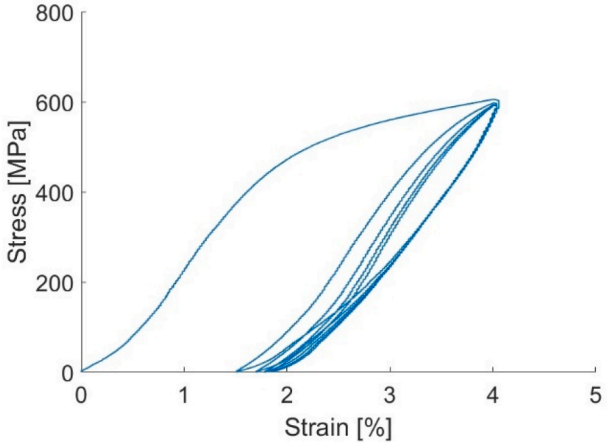

Fig. 15. Compression test at 4 % of AB F3 sample

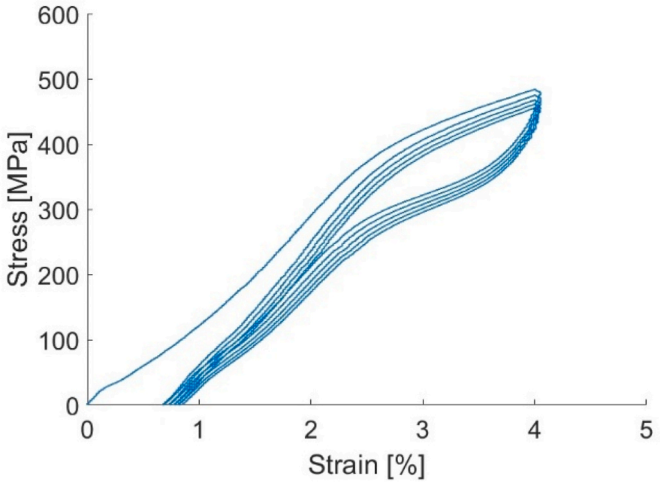

Fig. 16. Compression test at 4 % of AB F5 sample

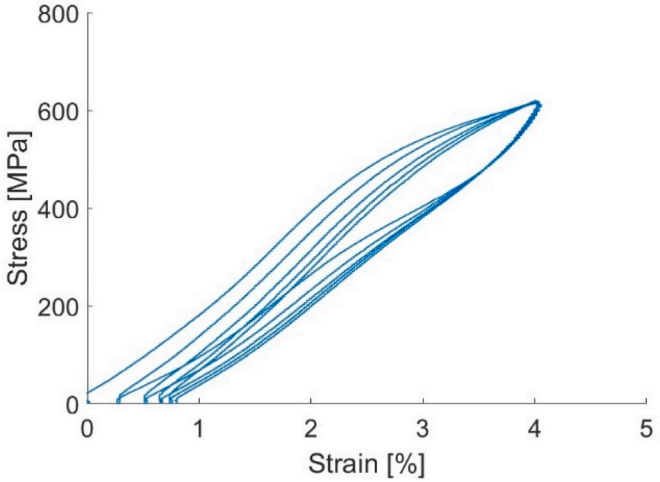

Fig. 17. Compression test at 4 % of HT F1 sample

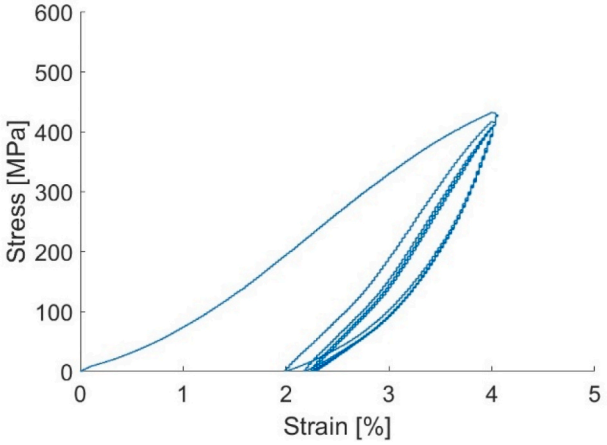

Fig. 18. Compression test at 4 % of HT F2 sample

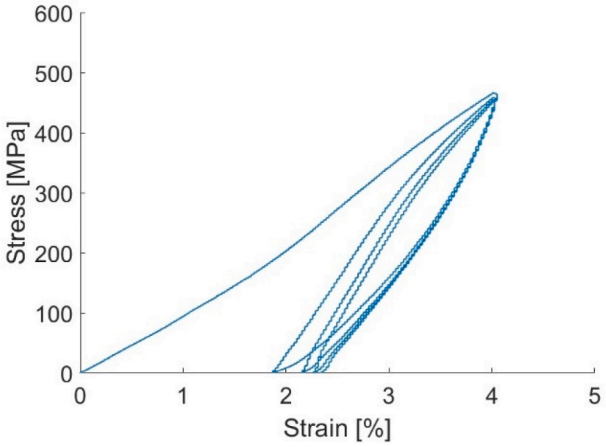

Fig. 19. Compression test at 4 % of HT F3 sample

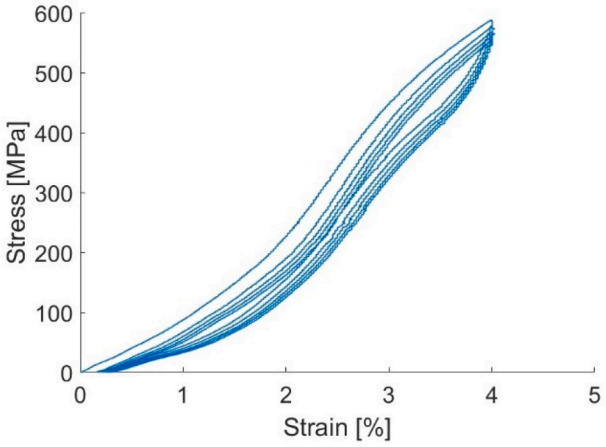

Fig. 20. Compression test at 4 % of HT F5 sample

References

[1] N. Shayesteh Moghaddam, et al., Achieving superelasticity in additively manufactured NiTi in compression without post-process heat treatment, Sci. Rep. 9 (1) (Dec. 2019), https://doi.org/10.1038/s41598-018-36641-4.

[2] A. Nespoli, et al., Towards an understanding of the functional properties of NiTi produced by powder bed fusion, Progress in Additive Manufacturing 6 (2) (May 2021) 321–337, https://doi.org/10.1007/s40964-020-00155-1.

[3] X. Wang, et al., Effect of process parameters on the phase transformation behavior and tensile properties of NiTi shape memory alloys fabricated by selective laser melting, Addit. Manuf. 36 (Dec) (2020), https://doi.org/10.1016/j.addma.2020.101545.

[4] S. Saedi, N. Shayesteh Moghaddam, A. Amerinatanzi, M. Elahinia, H.E. Karaca, On the effects of selective laser melting process parameters on microstructure and thermomechanical response of Ni-rich NiTi, Acta Mater. 144 (Feb. 2018) 552–560, https://doi.org/10.1016/j.actamat.2017.10.072.

[5] M. Jalali, et al., SLM additive manufacturing of NiTi porous implants: a review of constitutive models, finite element simulations, manufacturing, heat treatment, mechanical, and biomedical studies, Metals and Materials International. Korean Institute of Metals and Materials (2023), https://doi.org/10.1007/s12540-023-01401-1.

[6] J.N. Zhu, E. Borisov, X. Liang, E. Farber, M.J.M. Hermans, V.A. Popovich, Predictive analytical modelling and experimental validation of processing maps in additive manufacturing of nitinol alloys, Addit. Manuf. 38 (Feb) (2021), https://doi.org/10.1016/j.addma.2020.101802.

[7] L. Xue, et al., Controlling martensitic transformation characteristics in defect-free NiTi shape memory alloys fabricated using laser powder bed fusion and a process optimization framework, Acta Mater. 215 (Aug) (2021), https://doi.org/10.1016/j.actamat.2021.117017.

[8] S. Saedi, A.S. Turabi, M.T. Andani, C. Haberland, H. Karaca, M. Elahinia, The influence of heat treatment on the thermomechanical response of Ni-rich NiTi alloys manufactured by selective laser melting, J. Alloys Compd. 677 (Aug. 2016) 204–210, https://doi.org/10.1016/j.jallcom.2016.03.161.

[9] S. Saedi, A.S. Turabi, M.T. Andani, N.S. Moghaddam, M. Elahinia, H.E. Karaca, Texture, aging, and superelasticity of selective laser melting fabricated Ni-rich NiTi alloys, Mater. Sci. Eng., A 686 (Feb. 2017) 1–10, https://doi.org/10.1016/j.msea.2017.01.008.

[10] J. Van Humbeeck, Damping capacity of thermoelastic martensite in shape memory alloys, J. Alloys Compd. (Jun. 2003) 58–64, https://doi.org/10.1016/S0925-8388(03)00268-8.

[11] A. Nespoli, P. Bettini, E. Villa, G. Sala, F. Passaretti, A.M. Grande, A study on damping property of NiTi elements produced by selective laser-beam melting, Adv. Eng. Mater. 23 (6) (Jun. 2021), https://doi.org/10.1002/adem.202001246.

[12] A. Jahadakbar, et al., Design, modeling, additive manufacturing, and polishing of stiffness-modulated porous nitinol bone fixation plates followed by thermomechanical and composition analysis, Metals 10 (1) (Jan. 2020), https://doi.org/10.3390/met10010151.

[13] F. Bartolomeu, M.M. Costa, N. Alves, G. Miranda, F.S. Silva, Engineering the elastic modulus of NiTi cellular structures fabricated by selective laser melting, J. Mech. Behav. Biomed. Mater. 110 (Oct) (2020), https://doi.org/10.1016/j.jmbbm.2020.103891.

[14] T.W. Duerig, A.R. Pelton, Materials Properties Handbook: Titanium Alloys, ASM INTERNATIONAL, Materials Park, OH, 1994, pp. 1035–1048.

[15] F. Auricchio, R.L. Taylorb, Computer Methods in Applied Mechanics and Englnserlng Shape-Memory Alloys: Modelling and Numerical Simulations of the Finite-Strain Superelastic Behavior, 1997.

[16] S.E. Brika, M. Letenneur, C.A. Dion, V. Brailovski, Influence of particle morphology and size distribution on the powder flowability and laser powder bed fusion manufacturability of Ti-6Al-4V alloy, Addit. Manuf. 31 (Jan. 2020), https://doi.org/10.1016/j.addma.2019.100929.

[17] C. Pleass, S. Jothi, Influence of powder characteristics and additive manufacturing process parameters on the microstructure and mechanical behaviour of Inconel 625 fabricated by Selective Laser Melting, Addit. Manuf. 24 (Dec. 2018) 419–431, https://doi.org/10.1016/j.addma.2018.09.023.

[18] K. Otsuka, X. Ren, Physical metallurgy of Ti-Ni-based shape memory alloys, in: Progress in Materials Science, vol. 50, Elsevier Ltd, 2005, pp. 511–678, https://doi.org/10.1016/j.pmatsci.2004.10.001, 5.

[19] E. Borisov, K. Starikov, A. Popovich, T. Tihonovskaya, Investigation of the possibility of tailoring the chemical composition of the NiTi alloy by selective laser melting, Metals 11 (9) (Sep. 2021), https://doi.org/10.3390/met11091470.
[20] J. Michutta, C. Somsen, A. Yawny, A. Dlouhy, G. Eggeler, Elementary martensitic transformation processes in Ni-rich NiTi single crystals with Ni4Ti3 precipitates, Acta Mater. 54 (13) (Aug. 2006) 3525–3542, https://doi.org/10.1016/j.actamat.2006.03.036.
[21] R.F. Hamilton, T.A. Palmer, B.A. Bimber, Spatial characterization of the thermal-induced phase transformation throughout as-deposited additive manufactured NiTi bulk builds, Scripta Mater. 101 (May 2015) 56–59, https://doi.org/10.1016/j.scriptamat.2015.01.018.
[22] M. Elahinia, N. Shayesteh Moghaddam, M. Taheri Andani, A. Amerinatanzi, B. A. Bimber, R.F. Hamilton, Fabrication of NiTi through additive manufacturing: a review, in: Progress in Materials Science, vol. 83, Elsevier Ltd, Oct. 01, 2016, pp. 630–663, https://doi.org/10.1016/j.pmatsci.2016.08.001.
[23] E. Farber, J.N. Zhu, A. Popovich, V. Popovich, A review of NiTi shape memory alloy as a smart material produced by additive manufacturing, in: Materials Today: Proceedings, Elsevier Ltd, 2019, pp. 761–767, https://doi.org/10.1016/j.matpr.2020.01.563.
[24] J. Lee, Y.C. Shin, Effects of composition and post heat treatment on shape memory characteristics and mechanical properties for laser direct deposited nitinol, Lasers in Manufacturing and Materials Processing 6 (1) (Mar. 2019) 41–58, https://doi.org/10.1007/s40516-019-0079-5.
[25] D. Rigamonti, A. Nespoli, E. Villa, F. Passaretti, Implementation of a constitutive model for different annealed superelastic SMA wires with rhombohedral phase, Mech. Mater. 112 (Sep. 2017) 1339–1351, https://doi.org/10.1016/j.mechmat.2017.06.001.
[26] K. Khanlari, et al., Printing of NiTinol parts with characteristics respecting the general microstructural, compositional and mechanical requirements of bone replacement implants, Mater. Sci. Eng., A 839 (Apr) (2022), https://doi.org/10.1016/j.msea.2022.142839.
[27] S. Wang, et al., Role of porosity defects in metal 3D printing: formation mechanisms, impacts on properties and mitigation strategies, in: Materials Today, vol. 59, Elsevier B.V., Oct. 01, 2022, pp. 133–160, https://doi.org/10.1016/j.mattod.2022.08.014.
[28] X. Zhang, H. Zheng, W. Yu, A review on solidification cracks in high-strength aluminum alloys via laser powder bed fusion, Mater. Today: Proc. 70 (Jan. 2022) 465–469, https://doi.org/10.1016/j.matpr.2022.09.366.
[29] P. Sedmák, P. Šittner, J. Pilch, C. Curfs, Instability of cyclic superelastic deformation of NiTi investigated by synchrotron X-ray diffraction, Acta Mater. 94 (Aug. 2015) 257–270, https://doi.org/10.1016/j.actamat.2015.04.039.
[30] R. Delville, B. Malard, J. Pilch, P. Sittner, D. Schryvers, Transmission electron microscopy investigation of dislocation slip during superelastic cycling of Ni-Ti wires, Int. J. Plast. 27 (2) (Feb. 2011) 282–297, https://doi.org/10.1016/j.ijplas.2010.05.005.
[31] S. Miyazaki, T. Imai, Y. Igo, and K. Otsuka, “Effect of Cyclic Deformation on the Pseudoelasticity Characteristics of Ti-Ni Alloys.”.